

Impact of Stealthy Hyperuniform Magnetic Impurity Configurations on Bulk Magnetism in a Two-dimensional Heisenberg Model

Kota Asakura,* Kazuki Yamamoto, and Akihisa Koga

Department of Physics, Institute of Science Tokyo, Meguro, Tokyo 152-8551, Japan

(Dated: February 27, 2026)

We investigate an antiferromagnetic quantum Heisenberg model on a square lattice with high-spin magnetic impurities to clarify how random and stealthy hyperuniform impurity configurations influence the bulk magnetic properties. Stealthy hyperuniform configurations are generated using generalized cost functions that interpolate between square-lattice-like and triangular-lattice-like arrangements. Using linear spin-wave theory for the mixed-spin model, we demonstrate that triangular-lattice-like arrangements yield a larger average staggered magnetization than both random and square-lattice-like cases. This enhancement originates from sublattice effects: while the square-lattice-like configuration enforces nearest-neighbor impurities to occupy opposite sublattices due to its bipartite structure, the triangular-lattice-like arrangement allows same-sublattice nearest-neighbor pairs, thereby strengthening cooperative magnetic enhancement.

I. INTRODUCTION

Quantum spin systems have been intensively studied since the discovery of high-temperature superconductivity and are known to exhibit a wide variety of magnetic phases driven by quantum fluctuations. In particular, mixed-spin systems have attracted growing interest since they host magnetic properties that do not arise in uniform-spin models. Indeed, existing compounds such as magnetite Fe_3O_4 [1], spinel ferrites $M\text{Fe}_2\text{O}_4$ ($M=\text{Co}, \text{Mg}, \text{Mn}, \text{Zn}, \text{etc.}$) [2], double perovskite compounds [3], and mixed-spin chain compounds $R_2\text{BaNiO}_5$ ($R=\text{Nd}, \text{Pr}$) [4–6] provide representative realizations of such mixed-spin systems. Previous theoretical studies have largely focused on single-impurity problems [7–12] or idealized periodic systems [13–28], whereas the impact of impurity configurations has received less systematic attention.

More recently, high-entropy oxides, characterized by the random intermixing of multiple magnetic ions, have attracted broad attention since they exhibit strong compositional disorder and provide a prominent experimental platform for studying mixed-spin systems [29–33]. These compounds have been extensively studied for their magnetic behavior [34, 35], reversible energy storage capabilities [36–38], exceptionally high dielectric constants [39], electrostatic charge transfer [40], and catalytic performance [41]. Although the magnetic ions in high-entropy oxides are randomly distributed, some of them are known to exhibit antiferromagnetic order [42, 43]. These materials highlight the importance of understanding how spatially inhomogeneous spin configurations influence magnetic order. However, the randomness inherent in high-entropy oxides limits systematic control of spatial correlations. Thus, it is highly desirable to systematically clarify how the spatial configurations of magnetic ions (impurities) affect magnetic properties.

The concept of hyperuniformity [44, 45] provides a useful and systematic framework for classifying point distributions based on their long-range behavior. The point configuration is called hyperuniform if its variance in a large length scale

is smaller than a volume law. The periodic and quasiperiodic point configurations are hyperuniform, and their order metrics, which measure the degree of the regularity of the point configuration, have been examined [44–48]. Disordered hyperuniform point patterns have been actively investigated in recent years and are known to appear in a variety of fields such as soft matter [49, 50], solids [51, 52], active matter [53], biology [54], and cosmology [55]. A particularly useful subclass is the stealthy hyperuniform (SHU) system, characterized by the structure factor $S(\mathbf{k}) = 0$ for $0 < |\mathbf{k}| \leq K$ [56–58], where K is a certain cutoff parameter. It remains unclear whether the unique geometric correlations of SHU structures can induce local magnetic ordering in mixed-spin systems that is distinct from that in random configurations. So far, the SHU structures are known to influence physical properties in photonic materials [59–63], and their impact on quantum spin systems remains largely unexplored [64].

In our study, we consider an antiferromagnetic quantum Heisenberg model on a square lattice with high-spin magnetic impurities as a minimal theoretical setting. Using linear spin-wave theory, we take quantum fluctuations into account and study how their configurations affect the bulk staggered moments. We find that the average staggered magnetization is strongly affected by whether nearest-neighbor impurity pairs occupy the same or opposite sublattices, leading to either enhancement or suppression of the local magnetic moments depending on their relative positions. In contrast to random and square-lattice-like SHU arrangements, triangular-lattice-like SHU impurity configurations exhibit a larger staggered magnetization.

The paper is organized as follows. In Sec. II, we first introduce the mixed-spin antiferromagnetic Heisenberg model on a square lattice, and explain the spin-wave theory for evaluating magnetic properties. The procedures for generating SHU point patterns are also given. In Sec. III, we present the numerical results, analyzing the staggered magnetization for different impurity configurations. Finally, conclusions are given in Sec. IV.

* asakura@stat.phys.titech.ac.jp

II. MODEL AND METHODS

We consider the two-dimensional antiferromagnetic quantum Heisenberg model on a square lattice, which is described by the Hamiltonian

$$H = J \sum_{\langle ij \rangle} \mathbf{S}_i \cdot \mathbf{S}_j, \quad (1)$$

where \mathbf{S}_i denotes the spin operator at site i . Here, J is the antiferromagnetic exchange coupling constant and the summation runs over all nearest-neighbor pairs $\langle ij \rangle$.

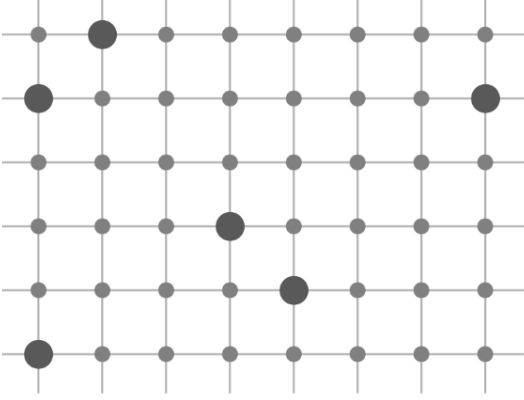


FIG. 1. Antiferromagnetic quantum Heisenberg model with higher-spin impurities.

In this paper, we study the effect of higher-spin magnetic impurities embedded in a conventional antiferromagnet on a square lattice with uniform spins $S = 1/2$, as shown in Fig. 1. Specifically, we introduce magnetic impurities with spin $S = 2$; that is, the local spin magnitude is taken as $S_i = 1/2$ for the host sites, and $S_i = 2$ for the impurity sites. To ensure that the antiferromagnetically ordered ground state is realized without a net uniform magnetization, the magnetic impurities are introduced in equal numbers on each sublattice. For the numerical calculations, we consider a spin system with $N = L \times L$ sites as a supercell, and construct a periodic structure by repeating this supercell, where L is the even number. Periodic boundary conditions are imposed with a period Ln , where n is a positive integer representing the number of supercells along each direction. In the following, the coordinate of a site is represented as $\mathbf{R}_i + \delta_m$, where \mathbf{R}_i is the coordinate of the i th supercell and δ_m is the relative coordinate of the m th site within the supercell.

To examine magnetic properties in the mixed-spin system, we use linear spin-wave theory based on the $1/S$ expansion. Specifically, we employ the Holstein-Primakoff transformation, where the spin operators are expressed for the sublattice A ,

$$S_{im}^z = S_m - a_{im}^\dagger a_{im}, \quad (2)$$

$$S_{im}^+ = \sqrt{2S_m - a_{im}^\dagger a_{im}} a_{im} \simeq \sqrt{2S_m} a_{im}, \quad (3)$$

and for the sublattice B ,

$$S_{im}^z = -S_m + a_{im}^\dagger a_{im}, \quad (4)$$

$$S_{im}^+ = a_{im}^\dagger \sqrt{2S_m - a_{im}^\dagger a_{im}} \simeq \sqrt{2S_m} a_{im}^\dagger, \quad (5)$$

where a_{im}^\dagger (a_{im}) creates (annihilates) a boson at the m th site in the i th supercell. Furthermore, we use the Fourier transform as

$$a_{im} = \frac{1}{n} \sum_{\mathbf{k}} a_{k\mathbf{m}} \exp[i\epsilon_m \mathbf{k} \cdot (\mathbf{R}_i + \delta_m)] \quad (6)$$

where $\epsilon_m = +1(-1)$ when the site m belongs to the sublattice A (B) and the wave vector is defined as $\mathbf{k} = (k_x, k_y) = (2\pi n_x/(Ln), 2\pi n_y/(Ln))$ with $n_\alpha = 0, 1, 2, \dots, n-1$ ($\alpha = x, y$). To leading order, the Hamiltonian eq. (1) reads

$$H = \sum_{\mathbf{k}} \begin{pmatrix} \mathbf{a}_{\mathbf{k}}^\dagger & \mathbf{a}_{\mathbf{k}} \end{pmatrix} \begin{pmatrix} h & \Delta_{\mathbf{k}} \\ \Delta_{\mathbf{k}}^\dagger & h \end{pmatrix} \begin{pmatrix} \mathbf{a}_{\mathbf{k}} \\ \mathbf{a}_{\mathbf{k}}^\dagger \end{pmatrix} \quad (7)$$

where $\mathbf{a}_{\mathbf{k}} = (a_{k1} \ a_{k2} \ \dots \ a_{kN})^t$. Diagonal matrix h is given as

$$h_{mn} = \frac{1}{2} \delta_{mn} \sum_{l \in \text{NN}(m)} S_l, \quad (8)$$

where $\text{NN}(m)$ denotes the set of nearest-neighbor sites of site m , and

$$(\Delta_{\mathbf{k}})_{mn} = \frac{1}{2} \sum_{\mathbf{d} \in \text{NN}(m \rightarrow n)} \sqrt{S_m S_n} e^{i\epsilon_m \mathbf{k} \cdot \mathbf{d}} \quad (9)$$

where \mathbf{d} is the displacement vectors from site m to a nearest-neighbor site n .

To diagonalize the quadratic bosonic Hamiltonian in Eq. (7), we perform a Bogoliubov transformation:

$$\begin{pmatrix} \mathbf{a}_{\mathbf{k}} \\ \mathbf{a}_{\mathbf{k}}^\dagger \end{pmatrix} = \begin{pmatrix} u_{\mathbf{k}} & v_{\mathbf{k}}^* \\ v_{\mathbf{k}} & u_{\mathbf{k}}^* \end{pmatrix} \begin{pmatrix} \mathbf{b}_{\mathbf{k}} \\ \mathbf{b}_{\mathbf{k}}^\dagger \end{pmatrix}, \quad (10)$$

where $\mathbf{b}_{\mathbf{k}} = (b_{k1} \ b_{k2} \ \dots \ b_{kN})^t$ and b_{km} (b_{km}^\dagger) denotes the annihilation (creation) operator of the quasiparticle, and $u_{\mathbf{k}}$ and $v_{\mathbf{k}}$ are the $N \times N$ matrices. Details of the diagonalization procedure are given in Appendix A. Then, we obtain

$$H = \sum_{\mathbf{k}\mathbf{m}} \omega_{\mathbf{k}\mathbf{m}} b_{\mathbf{k}\mathbf{m}}^\dagger b_{\mathbf{k}\mathbf{m}}, \quad (11)$$

where $\omega_{\mathbf{k}\mathbf{m}}$ is the quasiparticle excitation energy.

Taking the expectation value with respect to the ground state of the Hamiltonian eq. (11), we obtain the magnetization at site m within a unit cell given by

$$\langle S_{im}^z \rangle = \epsilon_m \left[S_m - \left(\frac{L}{2\pi} \right)^2 \int d\mathbf{k} \sum_n |(v_{\mathbf{k}})_{mn}|^2 \right]. \quad (12)$$

Using this local magnetization, the spatially-averaged staggered magnetization is given as

$$M_{\text{AF}} = \frac{1}{Nn^2} \sum_{im} \epsilon_m \langle S_{im}^z \rangle. \quad (13)$$

Diagonalizing the spin Hamiltonian, we examine bulk magnetic properties of an infinite system constructed by periodically repeating the supercell.

A. Spatical configurations of magnetic impurities

In this study, we discuss how the spatial configurations of the magnetic impurities affect bulk magnetic properties in the mixed-spin model. The magnetic impurities in the supercell are located by $\mathbf{r}_\ell^{(\gamma)}$ with the sublattice γ . The structure factor is then defined by [65]

$$S(\mathbf{k}) = \frac{1}{N'} \left| \sum_{\gamma} \rho_{\gamma}(\mathbf{k}) \right|^2, \quad (14)$$

$$\rho_{\gamma}(\mathbf{k}) = \sum_{\ell} e^{i\mathbf{k} \cdot \mathbf{r}_\ell^{(\gamma)}}. \quad (15)$$

where N' is the number of magnetic impurities in the supercell, and $\rho_{\gamma}(\mathbf{k})$ is the Fourier transform of the coordinates of the magnetic impurities in the sublattice γ . When periodic boundary conditions are imposed on the supercell, the allowed component of \mathbf{k} is given by $k_{\alpha} = 2\pi n_{\alpha}/L$ with integers $n_{\alpha} (\alpha = x, y)$.

To generate a point pattern with a certain structure factor, we introduce the objective function $\Phi (\geq 0)$, given by

$$\Phi (\{\mathbf{r}^{(A)}\}, \{\mathbf{r}^{(B)}\}) = \sum_{\mathbf{k}} V(\mathbf{k}) [S(\mathbf{k}) - S_{\text{target}}(\mathbf{k})]^2, \quad (16)$$

where $S_{\text{target}}(\mathbf{k})$ is the target structure factor, and $V(\mathbf{k})$ is the window function. By minimizing the objective function with respect to $\{\mathbf{r}^{(A)}\}$ and $\{\mathbf{r}^{(B)}\}$, one can obtain the point pattern corresponding to the target structure factor.

In this study, we focus on the SHU point patterns, which are characterized by $S(\mathbf{k}) = 0$ for $0 < |\mathbf{k}| \leq K$. The target structure factor and window function are given as $S_{\text{target}}(\mathbf{k}) = 0$ and $V_K(\mathbf{k}) = \theta(K - |\mathbf{k}|)$ with K is some positive number and $\theta(x)$ is the Heaviside step function. It is known that when K increases, points tend to separate from each other, and the nearest-neighbor interpoint distance becomes larger and more uniform. For sufficiently large K , long-wavelength (long-range) density fluctuations for the point pattern are suppressed, and the resulting configuration approaches a triangular-lattice-like ordering within the finite supercell, which is qualitatively similar to the point distribution obtained in continuous space [66].

To discuss how the configuration of magnetic impurities affects the bulk magnetization, we also consider an alternative objective function which confines the magnetic impurities to a single sublattice γ . The objective function is defined as

$$\Phi_{\gamma} (\{\mathbf{r}_\ell^{(\gamma)}\}) = \sum_{\mathbf{k}} V_{K_{\gamma}}(\mathbf{k}) [S_{\gamma}(\mathbf{k}) - S_{\text{target}}(\mathbf{k})]^2, \quad (17)$$

where $S_{\gamma} (= 2|\rho_{\gamma}|^2/N')$ is the structure factor for the magnetic impurities in the sublattice γ . Using this definition, one can consider the total cost function as

$$\Psi = (1 - c)\Phi + c \sum_{\gamma} \Phi_{\gamma} \quad (18)$$

where c is a constant. When $c = 0$ and K is large, minimizing the cost function drives the magnetic impurities to

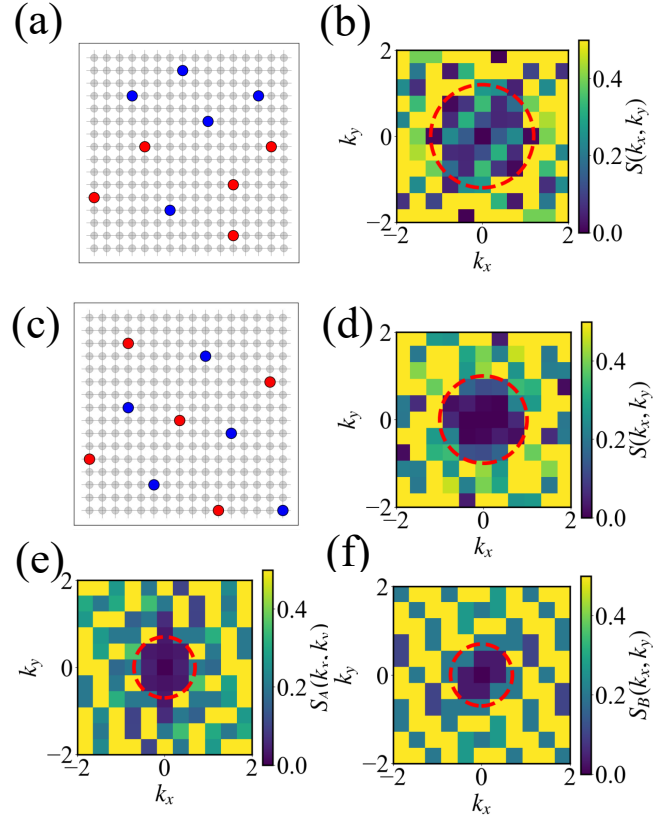


FIG. 2. (a) SHU impurity configurations (I). Large red and blue circles represent impurities in the sublattices A and B , respectively. The gray circles represent $S = 1/2$ host spins. (b) Structure factor $S(\mathbf{k})$ of the configuration (I). Dashed line indicates the boundary of the window function. (c) SHU impurity configurations (II) and its structure factors (d) $S(\mathbf{k})$, (e) $S_A(\mathbf{k})$, and (f) $S_B(\mathbf{k})$.

separate from each other, resulting in a triangular-lattice-like spatial configuration. The impurity configuration for $c = 0$ and $K = 1.2$ is referred to as the configuration (I). When $c = 1/2$, and K and K_{γ} are large, the cost function additionally favors spatial separation among impurities within the same sublattice. In this case, the resulting impurity arrangement becomes square-lattice-like. The impurity configuration for $c = 1/2$, $K = 1.1$, and $K_A = K_B = 0.8$ is referred to as configuration (II). Configurations (I) and (II) are schematically shown in Fig. 2. This cost function allows us to account for not only the stealthiness of the magnetic impurities as a whole but also the stealthiness of impurity distributions within each sublattice.

Before discussing the effects of impurity configurations, we first examine how a single magnetic impurity affects the magnetic properties of the $S = 1/2$ quantum Heisenberg model. To this end, we consider the $S = 1/2$ quantum Heisenberg model with $L = 16$, into which two isolated $S = 2$ spins are introduced as magnetic impurities. This allows us to maintain a zero total uniform magnetization within spin-wave theory while focusing on the local physics of a single impurity. The local magnetization profile around one of the magnetic

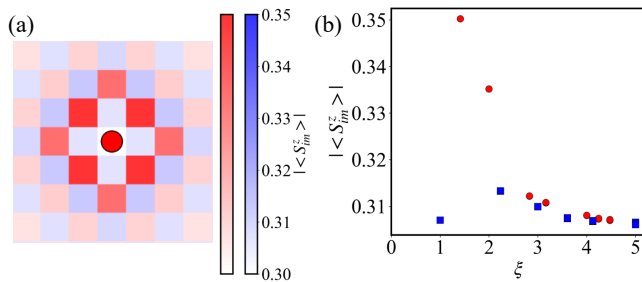


FIG. 3. (a) Local magnetization profile around an isolated magnetic impurity. A red circle denotes the $S = 2$ spin. The magnitude of the magnetic moment is represented by the density plot, with red (blue) corresponding to the same (opposite) sublattice as the impurity site. (b) Squares (circles) represent the magnitudes of the local magnetization in the same (opposite) sublattice as an isolated impurity as a function of the distance ξ from the impurity site.

impurities is shown in Fig. 3(a). We find that the magnetic moment at the $S = 2$ impurity site is renormalized down to approximately 1.47, which is significantly smaller than the value ~ 1.8 obtained for a quantum Heisenberg antiferromagnet with a uniform spin $S = 2$. This substantial reduction reflects quantum fluctuations originating from the surrounding $S = 1/2$ spin background. In contrast to the $S = 2$ impurity spins, the moments for the surrounding $S = 1/2$ spins become larger due to quantum fluctuations. In fact, enhanced magnetic moments are observed in the vicinity of the impurity, particularly on nearby sites belonging to the same sublattice as the impurity site. In contrast, when the nearest-neighbor sites of the impurity belong to the opposite sublattice, the magnetic moments remain nearly unchanged. This behavior is clearly illustrated in Fig. 3(b), where the magnetization on the same sublattice exhibits a strong distance dependence from the impurity, whereas that on the opposite sublattice shows only a weak dependence. Thus, a higher-spin impurity generates sublattice-dependent magnetic correlations extending over several lattice spacings [7, 8, 12]. This observation implies that the relative sublattice positions of multiple impurities should play an important role in determining the magnetic properties when a finite impurity concentration is introduced.

III. CONFIGURATION DEPENDENCE IN THE MAGNETIZATION PROFILE

In this section, we focus on dispersed impurity configurations in the system with $L = 16$, fixing the impurity concentration at $10/256$. Magnetization profiles for the random and SHU configurations (I) and (II) are shown in Figs. 4(a), (b), and (c). When the magnetic impurities are spatially well separated, local magnetic structures similar to those induced by a single impurity as discussed above emerge in the vicinity of each impurity. Namely, sublattice-dependent magnetic correlations develop locally around individual impurity sites. We therefore focus on how these local responses combine to form cooperative magnetic correlations. In the system with randomly distributed impurities, both the distances between im-

purities and the sublattices of nearest-neighbor impurities depend on the local spatial arrangement. As a result, magnetic correlations are locally enhanced in some regions, while they are suppressed in others, as shown in Fig. 4(a). On the other hand, in the SHU impurity configuration, the distances between nearest-neighbor impurities are nearly uniform. In this case, the sublattice arrangement of nearest-neighbor impurities becomes the dominant factor controlling the cooperative magnetic response. In the configuration (I), the triangular-lattice-like structure appears in the impurity distribution. In this case, nearest-neighbor impurity pairs sometimes belong to the same sublattice, which strongly enhances magnetic correlations between these impurities, as shown in Fig. 4(b). This leads to an overall enhancement of the magnetization. By contrast, in configuration (II), the magnetic impurities are located on square-lattice-like sites. In this case, magnetic correlations are not cooperatively enhanced since nearest-neighbor impurity pairs belong to distinct sublattices, as shown in Fig. 4(c).

The above results for the systems with dispersed impurity configurations demonstrate that the sublattice structure of nearest-neighbor impurities plays an important role in enhancing magnetic correlations throughout the system. Motivated by this result, one might expect that the larger staggered magnetization is realized in the clustered structure. To examine this expectation, we consider two clustered configurations with the same impurity concentration. Local magnetization profiles are shown in Figs. 4(d) and (e). When all magnetic impurities are clustered, enhanced magnetization appears only in the vicinity of the cluster, while little enhancement is observed away from it, as shown in Fig. 4(d). This behavior indicates that the large magnetic moments in the cluster, composed of $S = 2$ spins, tend to partially screen each other due to quantum fluctuations, resulting in suppressed magnetic correlations away from the cluster. Similar suppressions are clearly observed when two adjacent magnetic impurities are introduced into the spin system. In this case, their magnetic moments are strongly reduced ~ 1.2 , and little enhancement is observed outside the $S = 2$ dimer (not shown). This is analogous to the well-known fact that a magnetic dipole produces only a tiny magnetic field at long distances. Therefore, this clustered impurity configuration leads to a small bulk staggered magnetization.

By contrast, in a clustered system where each cluster is composed of impurities belonging to only one sublattice, magnetic correlations are cooperatively enhanced both inside and around the clusters, as shown in Fig. 4(e). This leads to a significantly larger bulk staggered magnetization of $M = 0.39$. These results demonstrate that clustering alone is not sufficient to maximize the average staggered magnetization; rather, the sublattice-dependent arrangement of impurities is essential for achieving cooperative magnetic enhancement across the system.

Next, we examine the statistical properties of the bulk staggered magnetization over independent impurity configurations. Figure 5 shows the histogram of the staggered magnetization in quantum spin systems with randomly distributed impurities and SHU configurations (I) and (II). We find that the staggered magnetization is widely distributed

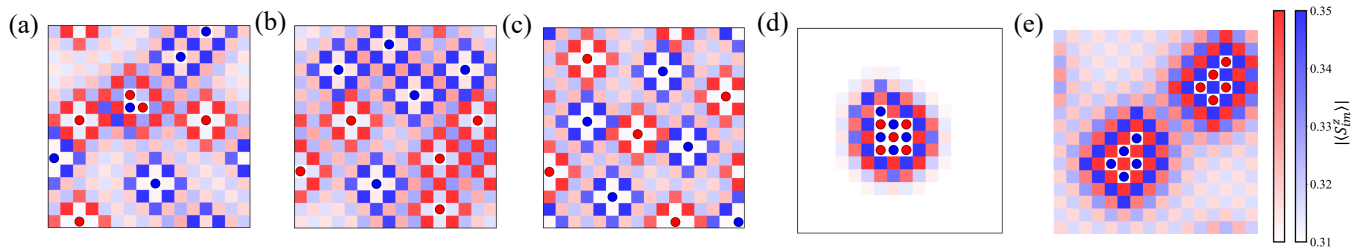


FIG. 4. Magnetization profiles of the spin system on a 16×16 square lattice with 10 impurities arranged in (a) a random configuration, (b) configuration (I), and (c) configuration (II). Panels (d) and (e) show the results for systems with clustered impurity configurations. Red (blue) circles denote $S = 2$ spins on sublattice A (B). The magnitude of the local magnetic moment is represented by the density plot, with red (blue) corresponding to sublattice A (B).

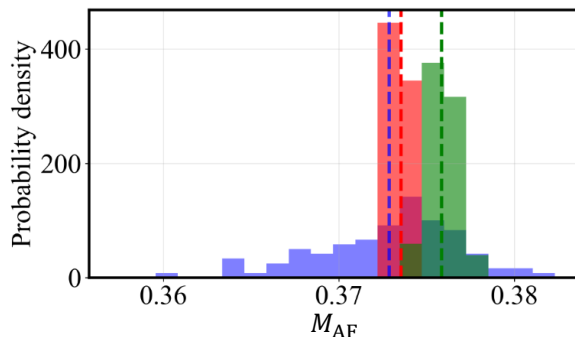


FIG. 5. Normalized histograms of the average sublattice magnetization M_{AF} for random and SHU impurity configurations. Comparison between random point patterns (blue, 100 samples) and SHU configuration (I) (green, 40 samples). Dashed lines indicate the corresponding mean values. Comparison between random point patterns (blue, 100 samples) and SHU configuration (II) (red, 40 samples).

for the random impurity configurations since the magnetic properties strongly depend on the specific impurity realization. The average value is $M_{AF} = 0.3729$ with a standard deviation $\sigma = 0.0041$. By contrast, in the SHU configurations, the distances between nearest-neighbor impurities are nearly identical, and all samples share similar structural properties. Configuration (I) nevertheless exhibits a larger sample-averaged staggered magnetization with $M_{AF} = 0.3759$ and $\sigma = 0.001$. In the system with SHU configuration (II), where the square-lattice-like impurity arrangement is realized, the staggered magnetization is much more narrowly distributed, with $M_{AF} = 0.3735$ and $\sigma = 0.0004$. These results can be understood as follows. In the triangular-lattice-like configuration, impurities are arranged at nearly uniform distances, and nearest-neighbor pairs are not constrained to belong to opposite sublattices. This allows same-sublattice impurity pairs to form, leading to a cooperative enhancement of the average staggered magnetization. In contrast, the square-lattice-like configuration, despite its nearly uniform impurity spacing, enforces opposite-sublattice nearest-neighbor pairs due to its bipartite structure. Consequently, such cooperative enhancement does not occur. In the random configuration, short-distance impurity pairs may appear on either the same or op-

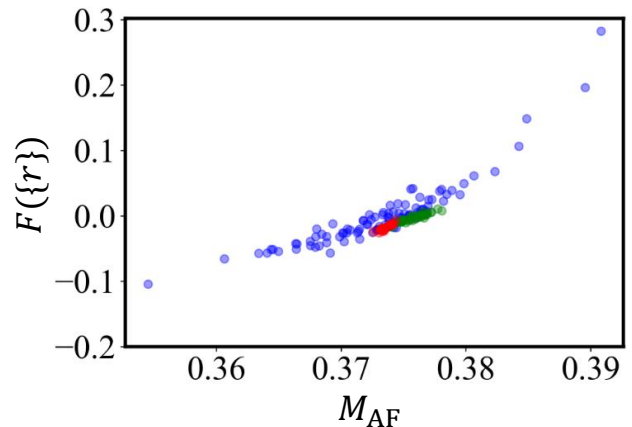


FIG. 6. Relationship between the average sublattice magnetization M_{AF} and the quantity $F(\{\mathbf{r}\})$ [see Eq. (19)]. Blue, green, and red circles represent the results for random configurations, configurations (I) and configuration (II).

posite sublattices. Because these enhancing and suppressing effects occur with comparable probability, they statistically compensate each other, resulting in an average magnetization similar to that of the square-lattice-like configuration.

We clarify how the average sublattice magnetization correlates with spatial configurations among $S = 2$ impurity spins. Here, we define a quantity characterizing the spatial configuration of the $S = 2$ impurities as

$$F(\{\mathbf{r}\}) = \frac{2}{N_2(N_2 - 1)} \sum_{\langle i, j \rangle} \epsilon_i \epsilon_j \exp\left[-\frac{1}{2} \left(\frac{r_{ij}}{2}\right)^2\right], \quad (19)$$

where \mathbf{r}_i is the coordinate of the i th impurity, N_2 is the total number of $S = 2$ impurities, and $r_{ij} = |\mathbf{r}_i - \mathbf{r}_j|$. The quantity takes larger values when spins belonging to the same sublattice, both with magnitude $S = 2$, are located close to each other, reflecting strong short-range alignment within the sublattice. Conversely, if spins with $S = 2$ from different sublattices are close to each other, their contributions partially screen out, resulting in smaller values. Thus, this quantity serves as a measure of the averaged staggered magnetization

induced by the impurity configuration.

Figure 6 presents a scatter plot of this quantity obtained from independent samples for the random configurations, and the SHU configurations (I) and (II). First, we find that the values calculated for various impurity distributions collapse onto a single curve. This fact indicates that the curve captures the essential magnetic characteristics of the system. As M_{AF} increases, this quantity increases monotonically. Moreover, it is immediately seen that configuration (I) yields systematically larger average values than configuration (II), reflecting the stronger short-range correlations among same-sublattice impurities in configuration (I). This behavior is consistent with the fact that the averaged staggered magnetization is enhanced when impurities on the same sublattice are located close to each other. Although the present study is limited to relatively small system sizes and a single impurity density, the observed correlation between M_{AF} and $F(\{r\})$ suggests that the quantity provides a useful quantification of local spin correlations and can serve as a complementary tool for characterizing the spatial structure of mixed-spin systems. Overall, our results indicate that the magnetic properties can be systematically characterized from the spatial arrangement of magnetic impurities, which may serve as a guideline for designing systems with enhanced magnetic moments.

IV. CONCLUSIONS

We have investigated the effects of spatial impurity configurations in a mixed-spin antiferromagnetic Heisenberg model on a square lattice. By systematically comparing random and stealthy hyperuniform impurity arrangements within linear spin-wave theory, we demonstrated that stealthy hyperuniform configurations lead to a markedly reduced variance in the distribution of the staggered magnetization, indicating more uniform magnetic responses across impurity realizations. Moreover, we demonstrated that triangular-lattice-like stealthy hyperuniform configurations yield a larger average staggered magnetization than both random and square-lattice-like arrangements. This enhancement originates from the sublattice dependence of nearest-neighbor magnetic impurities: impurities located on the same sublattice cooperatively enhance local magnetic moments, whereas those on opposite sublattices suppress them. Our results highlight the importance of controlled spatial correlations in impurity configurations and demonstrate that hyperuniform structures provide a powerful framework for engineering magnetic properties in mixed-spin quantum systems.

ACKNOWLEDGMENTS

Parts of the numerical calculations were performed in the supercomputing systems in ISSP, the University of Tokyo. This work was supported by Grant-in-Aid for Scientific Research from JSPS, KAKENHI Grants No. JP25K17327 (K.Y.), JP22K03525, JP25H01521, and JP25H01398 (A.K.). This work was partly funded by Hirose Foundation, the Pre-

cise Measurement Technology Promotion Foundation, and the Fujikura Foundation.

Appendix A: Detailed calculation for the Bogoliubov transformation

In this appendix, we give the detailed calculation for choosing the matrix given in Eq. (10) in the Bogoliubov transformation. First, we define

$$H'_k = \begin{pmatrix} h & \Delta_k \\ \Delta_k^\dagger & h \end{pmatrix} \quad (\text{A1})$$

$$\tilde{H}_k = H'_k P = \begin{pmatrix} h & -\Delta_k \\ \Delta_k^\dagger & -h \end{pmatrix}. \quad (\text{A2})$$

where H'_k is the matrix given in Eq. (7), and

$$P = \text{diag}(\underbrace{1, \dots, 1}_N, \underbrace{-1, \dots, -1}_N). \quad (\text{A3})$$

We consider the following eigenvalue problem, which is necessary to diagonalize Eq. (A2):

$$\tilde{H}_k \Psi_{km} = \frac{\omega_{km}}{2} \Psi_{km}. \quad (\text{A4})$$

Here, we introduce a generalized inner product, which allows us to diagonalize the equation given in Eq. (A2). This generalized inner product is necessary because the standard inner product does not always guarantee the orthogonality or normalization of the eigenvectors:

$$\Psi_{km} \circ \Psi_{k,m'} \equiv \Psi_{km}^\dagger P \Psi_{k,m'}, \quad (\text{A5})$$

which satisfies

$$\begin{cases} (\Psi_{km} \circ \Psi_{k,m'})^\dagger &= \Psi_{k,m'} \circ \Psi_{km}, \\ \Psi_{km} \circ (\tilde{H}_k \Psi_{k,m'}) &= (\tilde{H}_k \Psi_{km}) \circ \Psi_{k,m'}. \end{cases} \quad (\text{A6})$$

Since the generalized inner product defined in Eq. (A5) does not fix the magnitude of the vectors, proper normalization and orthogonality condition must be imposed as follows:

$$\Psi_{km} \circ \Psi_{km} \equiv \begin{cases} \delta_{m,m'}, & \text{if } \omega_{k,m} > 0, \\ -\delta_{m,m'}, & \text{if } \omega_{k,m} < 0. \end{cases} \quad (\text{A7})$$

Regarding the eigenvalues ω_{km} , the Hamiltonian in Eq. (A2) always has real eigenvalues that are either positive or negative. To demonstrate this, we introduce the operator C to represent complex conjugation and define the block matrix M as

$$M = \begin{pmatrix} 0 & E \\ E & 0 \end{pmatrix}, \quad (\text{A8})$$

where E is the identity matrix. Then, we have

$$\tilde{H}_k (CM \Psi_{km}) = -CM \tilde{H}_k \Psi_{km} = -\frac{\omega_{km}}{2} (CM \Psi_{km}). \quad (\text{A9})$$

This shows that $CM\Psi_{k,m}$ is also an eigenvector of \tilde{H}_k with eigenvalue $-\omega_{km}/2$, demonstrating the symmetric structure of the eigenvalues. We also define the set of eigenvectors of \tilde{H} as V_k , which is given by

$$V_k = \left(\Psi_{k,1}, \dots, \Psi_{k,m}, \dots, \Psi_{k,N}, \right. \\ \left. CM\Psi_{k,1}, \dots, CM\Psi_{k,m}, \dots, CM\Psi_{k,N} \right). \quad (\text{A10})$$

which is a $2N \times 2N$ matrix. By using Eq. (A7), V_k satisfies the following generalized normalization and orthogonality condition

$$V_k^\dagger P V_k = P. \quad (\text{A11})$$

In order to perform the final step of the diagonalization procedure, we introduce the relation between V_k and Ω_k , where Ω_k is the diagonal matrix of eigenvalues obtained from the final diagonalization of H'_k in Eq. (A1):

$$\Omega_k = \text{diag} \left(\underbrace{\omega_{k,1}, \dots, \omega_{k,N}}_N, \underbrace{\omega_{k,1}, \dots, \omega_{k,N}}_N \right). \quad (\text{A12})$$

The relation between V_k and Ω_k is then given by

$$V_k \Omega_k P = \tilde{H}_k V_k. \quad (\text{A13})$$

Since we also require an explicit matrix form of the Bogoliubov transformation matrix in Eq. (10), we choose the matrix

U_k as

$$U_k = P V_k P. \quad (\text{A14})$$

We can determine the form of U_k based on Eq. (A10):

$$U_k = \begin{pmatrix} u_k & v_k^* \\ v_k & u_k^* \end{pmatrix}. \quad (\text{A15})$$

For convenience, we rewrite the vectors in Eq. (10) as

$$\Lambda_k = \begin{pmatrix} a_k \\ a_k^\dagger \end{pmatrix}, \quad (\text{A16})$$

$$\Gamma_k = \begin{pmatrix} b_k \\ b_k^\dagger \end{pmatrix}. \quad (\text{A17})$$

where a_k and b_k are bosonic operators, so U_k must satisfy a condition that preserves the bosonic commutation relations of Λ_k and Γ_k . This condition is expressed as

$$U_k^\dagger P U_k = U_k P U_k^\dagger = P. \quad (\text{A18})$$

This choice of the form of U_k in Eq. (A14) is made specifically to ensure that Eq. (A18) is automatically satisfied. By substituting Eqs. (10), (A2), and (A11)-(A18) to Eq. (7), we can diagonalize the Hamiltonian H'_k as

$$\Lambda_k^\dagger H'_k \Lambda_k = \Gamma_k^\dagger U_k^\dagger H'_k U_k \Gamma_k \\ = \Gamma_k^\dagger P V_k^\dagger P \tilde{H}_k P P V_k P \Gamma_k \\ = \Gamma_k^\dagger \Omega_k \Gamma_k, \quad (\text{A19})$$

By using Eq. (A14), we can derive the final diagonalization relation Eq. (A19) and also compute Eq. (12) in numerical calculations.

-
- [1] E. J. W. Verway, *Nature* **144**, 327 (1939).
[2] D. S. Mathew and R.-S. Juang, An overview of the structure and magnetism of spinel ferrite nanoparticles and their synthesis in microemulsions, *Chemical Engineering Journal* **129**, 51 (2007).
[3] S. Vasala and M. Karppinen, A2b'b"o6 perovskites: A review, *Progress in Solid State Chemistry* **43**, 1 (2015).
[4] V. Sachan, D. J. Buttrey, J. M. Tranquada, and G. Shirane, Neutron-scattering study of magnetism in $\text{Nd}_2\text{BaNiO}_5$, *Phys. Rev. B* **49**, 9658 (1994).
[5] A. Zheludev, J. M. Tranquada, T. Vogt, and D. J. Buttrey, Magnetic excitations and soft-mode transition in the quasi-one-dimensional mixed-spin antiferromagnet $\text{Pr}_2\text{BaNiO}_5$, *Phys. Rev. B* **54**, 6437 (1996).
[6] A. Zheludev, J. M. Tranquada, T. Vogt, and D. J. Buttrey, Magnetic excitations and soft-mode transition in $\text{Pr}_2\text{BaNiO}_5$, *Europhysics Letters* **35**, 385 (1996).
[7] V. N. Kotov, J. Oitmaa, and O. Sushkov, Magnetic impurity in the two-dimensional heisenberg antiferromagnet, *Phys. Rev. B* **58**, 8495 (1998).
[8] V. N. Kotov, J. Oitmaa, and O. Sushkov, Local magnetic impurities in the two-dimensional quantum heisenberg antiferromagnet, *Phys. Rev. B* **58**, 8500 (1998).
[9] K. H. Höglund and A. W. Sandvik, Impurity effects at finite temperature in the two-dimensional $s=1/2$ heisenberg antiferromagnet, *Phys. Rev. B* **70**, 024406 (2004).
[10] K. H. Höglund and A. W. Sandvik, Susceptibility of the 2d spin- $\frac{1}{2}$ heisenberg antiferromagnet with an impurity, *Phys. Rev. Lett.* **91**, 077204 (2003).
[11] A. Lüscher and O. P. Sushkov, Long-range dynamics of magnetic impurities coupled to a two-dimensional heisenberg antiferromagnet, *Phys. Rev. B* **71**, 064414 (2005).
[12] S. Shinkevich, O. F. Syljuåsen, and S. Eggert, Spin-wave calculation of the field-dependent magnetization pattern around an impurity in heisenberg antiferromagnets, *Phys. Rev. B* **83**, 054423 (2011).
[13] M. Fujii, S. Fujimoto, and N. Kawakami, Magnetic and critical properties of alternating spin chain with $s=1/2, 1$ in magnetic fields, *Journal of the Physical Society of Japan* **65**, 2381 (1996).
[14] S. K. Pati, S. Ramasesha, and D. Sen, Low-lying excited states and low-temperature properties of an alternating spin-1–spin- $1/2$ chain: A density-matrix renormalization-group study, *Phys. Rev. B* **55**, 8894 (1997).
[15] A. K. Kolezhuk, H.-J. Mikeska, and S. Yamamoto, Matrix-product-states approach to heisenberg ferrimagnetic spin

- chains, *Phys. Rev. B* **55**, R3336 (1997).
- [16] A. K. Kolezhuk, H.-J. Mikeska, K. Maisinger, and U. Schöllwöck, Spinon signatures in the critical phase of the $1, \frac{1}{2}$ ferrimagnet in a magnetic field, *Phys. Rev. B* **59**, 13565 (1999).
- [17] F. C. Alcaraz and A. L. Malvezzi, Critical behaviour of mixed heisenberg chains, *Journal of Physics A: Mathematical and General* **30**, 767 (1997).
- [18] S. Brehmer, H.-J. Mikeska, and S. Yamamoto, Low-temperature properties of quantum antiferromagnetic chains with alternating spins and, *Journal of Physics: Condensed Matter* **9**, 3921 (1997).
- [19] A. K. Kolezhuk, H.-J. Mikeska, and S. Yamamoto, Matrix-product-states approach to heisenberg ferrimagnetic spin chains, *Phys. Rev. B* **55**, R3336 (1997).
- [20] S. Yamamoto, S. Brehmer, and H.-J. Mikeska, Elementary excitations of heisenberg ferrimagnetic spin chains, *Phys. Rev. B* **57**, 13610 (1998).
- [21] A. Koga, S. Kumada, N. Kawakami, and T. Fukui, Mixed-spin ladders and plaquette spin chains, *J. Phys. Soc. Jpn.* **67**, 622 (1998).
- [22] S. Yamamoto and T. Fukui, Thermodynamic properties of heisenberg ferrimagnetic spin chains: Ferromagnetic-antiferromagnetic crossover, *Phys. Rev. B* **57**, R14008 (1998).
- [23] A. Koga, S. Kumada, and N. Kawakami, Quantum phase transitions in two-dimensional spin systems with ladder, plaquette and mixed-spin structures, *J. Phys. Soc. Jpn.* **68**, 2373 (1999).
- [24] T. Sakai and S. Yamamoto, Critical behavior of anisotropic heisenberg mixed-spin chains in a field, *Phys. Rev. B* **60**, 4053 (1999).
- [25] A. Koga and N. Kawakami, Phase diagram for two-dimensional spin systems with ladder, plaquette and mixed-spin structures, *J. Phys. Soc. Jpn.* **69**, 1834 (2000).
- [26] Y. Takushima, A. Koga, and N. Kawakami, Magnetic double structure for $s=1$ and $s=1/2$ mixed-spin systems, *Phys. Rev. B* **61**, 15189 (2000).
- [27] S. Yamamoto and T. Sakai, Multiplateau magnetization curves of one-dimensional heisenberg ferrimagnets, *Phys. Rev. B* **62**, 3795 (2000).
- [28] A. Koga and J. Nasu, Residual entropy and spin fractionalizations in the mixed-spin kitaev model, *Phys. Rev. B* **100**, 100404 (2019).
- [29] C. M. Rost, E. Sacht, T. Borman, A. Moballeggh, E. C. Dickey, D. Hou, J. L. Jones, S. Curtarolo, and J.-P. Maria, Entropy-stabilized oxides, *Nature Communications* **6**, 8485 (2015).
- [30] A. Sarkar, R. Kruk, and H. Hahn, Magnetic properties of high entropy oxides, *Dalton Trans.* **50**, 1973 (2021).
- [31] R. Witte, A. Sarkar, R. Kruk, B. Eggert, R. A. Brand, H. Wende, and H. Hahn, High-entropy oxides: An emerging prospect for magnetic rare-earth transition metal perovskites, *Phys. Rev. Mater.* **3**, 034406 (2019).
- [32] A. Mao, H.-X. Xie, H.-Z. Xiang, Z.-G. Zhang, H. Zhang, and S. Ran, A novel six-component spinel-structure high-entropy oxide with ferrimagnetic property, *Journal of Magnetism and Magnetic Materials* **503**, 166594 (2020).
- [33] A. R. Mazza, E. Skoropata, Y. Sharma, J. Lapano, T. W. Heitmann, B. L. Musico, V. Keppens, Z. Gai, J. W. Freeland, T. R. Charlton, M. Brahlek, A. Moreo, E. Dagotto, and T. Z. Ward, Designing magnetism in high entropy oxides, *Advanced Science* **9**, 2200391 (2022).
- [34] A. Mao, H.-Z. Xiang, Z.-G. Zhang, K. Kuramoto, H. Yu, and S. Ran, Solution combustion synthesis and magnetic property of rock-salt $(\text{co}_0.2\text{cu}_0.2\text{mg}_0.2\text{ni}_0.2\text{zn}_0.2)\text{o}$ high-entropy oxide nanocrystalline powder, *Journal of Magnetism and Magnetic Materials* **484**, 245 (2019).
- [35] P. B. Meisenheimer, T. J. Kratofil, and J. T. Heron, Giant enhancement of exchange coupling in entropy-stabilized oxide heterostructures, *Scientific Reports* **7**, 13344 (2017).
- [36] D. Bérardan, S. Franger, A. K. Meena, and N. Dragoë, Room temperature lithium superionic conductivity in high entropy oxides, *J. Mater. Chem. A* **4**, 9536 (2016).
- [37] A. Sarkar, L. Velasco, D. Wang, Q. Wang, G. Talasila, L. de Biasi, C. Kübel, T. Brezesinski, S. S. Bhattacharya, H. Hahn, and B. Breitung, High entropy oxides for reversible energy storage, *Nature Communications* **9**, 3400 (2018).
- [38] N. Qiu, H. Chen, Z. Yang, S. Sun, Y. Wang, and Y. Cui, A high entropy oxide $(\text{mg}_0.2\text{co}_0.2\text{ni}_0.2\text{cu}_0.2\text{zn}_0.2\text{o})$ with superior lithium storage performance, *Journal of Alloys and Compounds* **777**, 767 (2019).
- [39] D. Bérardan, S. Franger, D. Dragoë, A. K. Meena, and N. Dragoë, Colossal dielectric constant in high entropy oxides, *physica status solidi (RRL) – Rapid Research Letters* **10**, 328 (2016).
- [40] Z. Rak, C. M. Rost, M. Lim, P. Sarker, C. Toher, S. Curtarolo, J.-P. Maria, and D. W. Brenner, Charge compensation and electrostatic transferability in three entropy-stabilized oxides: Results from density functional theory calculations, *Journal of Applied Physics* **120**, 095105 (2016).
- [41] H. Chen, J. Fu, P. Zhang, H. Peng, C. W. Abney, K. Jie, X. Liu, M. Chi, and S. Dai, Entropy-stabilized metal oxide solid solutions as co oxidation catalysts with high-temperature stability, *J. Mater. Chem. A* **6**, 11129 (2018).
- [42] J. Zhang, J. Yan, S. Calder, Q. Zheng, M. A. McGuire, D. L. Abernathy, Y. Ren, S. H. Lapidus, K. Page, H. Zheng, J. W. Freeland, J. D. Budai, and R. P. Hermann, Long-range antiferromagnetic order in a rocksalt high entropy oxide, *Chemistry of Materials* **31**, 3705 (2019).
- [43] Y. Pu, D. Moseley, Z. He, K. C. Pitike, M. E. Manley, J. Yan, V. R. Cooper, V. Mitchell, V. K. Peterson, B. Johannessen, R. P. Hermann, and P. Cao, $(\text{mg}, \text{mn}, \text{fe}, \text{co}, \text{ni})\text{o}$: A rocksalt high-entropy oxide containing divalent mn and fe, *Science Advances* **9**, eadi8809 (2023), <https://www.science.org/doi/pdf/10.1126/sciadv.adi8809>.
- [44] S. Torquato and F. H. Stillinger, Local density fluctuations, hyperuniformity, and order metrics, *Phys. Rev. E* **68**, 041113 (2003).
- [45] S. Torquato, Hyperuniform states of matter, *Physics Reports* **745**, 1 (2018).
- [46] C. E. Zachary and S. Torquato, Hyperuniformity in point patterns and two-phase random heterogeneous media, *Journal of Statistical Mechanics: Theory and Experiment* **2009**, P12015 (2009).
- [47] C. Lin, P. J. Steinhardt, and S. Torquato, Hyperuniformity variation with quasicrystal local isomorphism class, *Journal of Physics: Condensed Matter* **29**, 204003 (2017).
- [48] A. Koga and S. Sakai, Hyperuniformity in two-dimensional periodic and quasiperiodic point patterns, *Phys. Rev. E* **109**, 044103 (2024).
- [49] L. Berthier, P. Chaudhuri, C. Coulais, O. Dauchot, and P. Sollich, Suppressed compressibility at large scale in jammed packings of size-disperse spheres, *Phys. Rev. Lett.* **106**, 120601 (2011).
- [50] R. Kurita and E. R. Weeks, Incompressibility of polydisperse random-close-packed colloidal particles, *Phys. Rev. E* **84**, 030401 (2011).
- [51] Y. Zheng, L. Liu, H. Nan, Z.-X. Shen, G. Zhang, D. Chen, L. He, W. Xu, M. Chen, Y. Jiao, and H. Zhuang, Disordered hyperuniformity in two-dimensional amorphous silica, *Sci. Adv.* **6**, eaba0826 (2020).

- [52] J. B. Llorens, I. Guillamón, I. G. Serrano, R. Córdoba, J. Sesé, J. M. De Teresa, M. R. Ibarra, S. Vieira, M. Ortuño, and H. Suderow, Disordered hyperuniformity in superconducting vortex lattices, *Phys. Rev. Res.* **2**, 033133 (2020).
- [53] M. Huang, W. Hu, S. Yang, Q.-X. Liu, and H. P. Zhang, Circular swimming motility and disordered hyperuniform state in an algae system, *Proc. Natl. Acad. Sci. U.S.A.* **118**, e2100493118 (2021).
- [54] Y. Jiao, T. Lau, H. Hatzikirou, M. Meyer-Hermann, J. C. Corbo, and S. Torquato, Avian photoreceptor patterns represent a disordered hyperuniform solution to a multiscale packing problem, *Phys. Rev. E* **89**, 022721 (2014).
- [55] A. Gabrielli, M. Joyce, and F. Sylos Labini, Glass-like universe: Real-space correlation properties of standard cosmological models, *Phys. Rev. D* **65**, 083523 (2002).
- [56] S. Torquato, G. Zhang, and F. H. Stillinger, Ensemble theory for stealthy hyperuniform disordered ground states, *Phys. Rev. X* **5**, 021020 (2015).
- [57] R. D. Batten, F. H. Stillinger, and S. Torquato, Classical disordered ground states: Super-ideal gases and stealth and equiluminous materials, *Journal of Applied Physics* **104**, 033504 (2008).
- [58] O. Leseur, R. Pierrat, and R. Carminati, High-density hyperuniform materials can be transparent, *Optica* **3**, 763 (2016).
- [59] M. Florescu, S. Torquato, P. J. Steinhardt, and P. M. Chaikin, Designer disordered materials with large, complete photonic band gaps, *Proc. Natl. Acad. Sci. U.S.A.* **106**, 20658 (2009).
- [60] L. S. Froufe-Pérez, M. Engel, P. F. Damasceno, N. Muller, J. Haberko, S. C. Glotzer, and F. Scheffold, Role of short-range order and hyperuniformity in the formation of band gaps in disordered photonic materials, *Phys. Rev. Lett.* **117**, 053902 (2016).
- [61] W. Man, M. Florescu, K. Matsuyama, P. Yadak, S. Torquato, P. Steinhardt, and P. Chaikin, Experimental observation of photonic bandgaps in hyperuniform disordered material, in *Conference on Lasers and Electro-Optics 2010* (Optica Publishing Group, 2010) p. CThS2.
- [62] W. Man, M. Florescu, E. P. Williamson, Y. He, S. R. Hashemizad, B. Y. Leung, D. R. Liner, S. Torquato, P. M. Chaikin, and P. J. Steinhardt, Isotropic band gaps and freeform waveguides observed in hyperuniform disordered photonic solids, *Proceedings of the National Academy of Sciences of the United States of America* **110**, 15886 (2013).
- [63] K. Asakura, K. Yamamoto, and A. Koga, Elliptical-rod geometries enhance photonic band gaps in disordered stealthy hyperuniform photonic crystals, *Journal of the Physical Society of Japan* **95**, 024711 (2026).
- [64] A. Bose and S. Torquato, Quantum phase transitions in long-range interacting hyperuniform spin chains in a transverse field, *Phys. Rev. B* **103**, 014118 (2021).
- [65] O. U. Uche, S. Torquato, and F. H. Stillinger, Collective coordinate control of density distributions, *Phys. Rev. E* **74**, 031104 (2006).
- [66] O. U. Uche, F. H. Stillinger, and S. Torquato, Constraints on collective density variables: Two dimensions, *Phys. Rev. E* **70**, 046122 (2004).